COMMUNICATION

Check for updates

Bimetallic alloy Ag@Au nanorings with hollow dual-rims focus near-field on circular intra-nanogaps†

Sungwoo Lee, [iD] ‡[ab] Insub Jung,‡[ab] Soohyun Lee,[a] Jaewon Lee,[a] Myeong Jin Oh,[a] Minsun Park,[a] MohammadNavid Haddadnezhad,[a] Woocheol Park[a] and Sungho Park [iD] *[a]

Here, we report a highly sensitive and reliable surface enhanced Raman scattering (SERS)-based immunoassay using bimetallic alloy Ag@Au hollow dual-rim nanorings (DRNs) where two hollow nanorings with different diameters are concentrically overlapped and connected by thin metal ligaments, forming circular hot-zones in the intra-nanogaps between the inner and outer rims. Pt DRNs were first prepared, and then Ag was deposited on the surface of the Pt skeleton, followed by Au coating, resulting in alloy Ag@Au hollow DRNs. The chemical stability of Au and the high optical properties of Ag are incorporated into a single entity, Ag@Au hollow DRNs, enabling strong single-particle SERS activity and biocompatibility through surface modification with thiol-containing functionalities. When Ag@Au hollow DRNs were utilized as nanoprobes for detecting human chorionic gonadotropin (HCG) hormone through a SERS-based immunoassay, a very low limit of detection of 10 pM with high reliability was achieved, strongly indicating their advantage as ultrasensitive SERS nanoprobes.

New concepts

Development of plasmonic nanoparticles with high structural complexity and controllability in a solution-phase is important for a myriad of applications, especially in biosensing where strong electromagnetic field confinement of optical nanotransducers is required. In this paper, we represent the on-demand multi-stepwise synthetic strategy of bimetallic alloy Ag@Au hollow dual-rim nanorings (DRNs) where two nanorings with different diameters are concentrically overlapped and connected by thin metal ligaments, forming circular hot-zones in the intra-nanogaps between the inner and outer rims, acting as a single nanoparticle SERS nanotransducer. Ag@Au hollow DRNs with high homogeneity both in size and shape were successfully synthesized through the consecutive application of Ag deposition and Au deposition on the Pt DRN skeleton. The chemical stability of Au and high optical properties of Ag are incorporated into a single entity, Ag@Au hollow DRNs, enabling a strong single-particle SERS activity and a biocompatibility through surface modification with thiol-containing functionalities. Ag@Au hollow DRNs show strong near-field focusing capability and high biocompatibility compared to single component (*i.e.*, pure Au or Ag) DRNs, and single-rim nanorings from the systematic investigation of surface-enhanced Raman spectroscopy. Our work demonstrates the importance of the combinatorial effect of plasmonic intra-nanogaps in a single entity with alloy components for SERS-based immunoassays.

Introduction

Constructing designer plasmonic nanocrystals with highly controlled shape and size has been of interest for elucidating unique and unprecedented structure-property relationships with light at the nanoscale and has spurred extensive research in a wide range of applications including energy, chemical- and biosensors and light-enhanced applications.[1–8] Localized surface plasmon resonance (LSPR) involves the collective oscillation of conducting free electrons of metallic nanoparticles, which is strongly influenced by the shape, size, and surrounding medium. Recently, plasmonic nanocrystals with diverse shapes

(*e.g.*, nanorods, nanocubes, nanobipyramids, and nanostars) have been synthesized, to fully exploit their plasmonic properties.[9] Among these, two-dimensional (2D) plasmonic nanorings (NRs) have shown great promise due to their large surface to volume ratio, inner open space, and tunable optical properties (from visible to near-IR windows) due to their anisotropy.[10–12] However, their structural simplicity (*i.e.*, single circular rim) has been a limitation in terms of near-field focusing capability.[13–15] Since electromagnetic fields are strongly confined within narrow gaps among adjacent metallic nanoparticles (NPs), introducing homogeneous intraparticle nanogaps with tunable gap distances in a single entity can be an effective strategy for obtaining strong, reproducible, and stable SERS signals.[16–18] In that regard, a plasmonic dual-rim nanoring (DRNs) architecture has recently

[a] *Department of Chemistry, Sungkyunkwan University, Suwon 16419, South Korea*
[b] *Institute of Basic Science, Sungkyunkwan University, Suwon 16419, South Korea*
‡ These authors contributed equally.

been proposed as an ideal light entrapper due to the tunable circular intra-nanogaps, which enables strong electromagnetic near-field focusing as well as effective analyte capturing at the inner voids.[13,19]

On the other hand, immunoassays have been utilized for the detection and quantification of target analytes in biological and clinical samples by harnessing specific immunochemical reactions between antibodies and antigens.[20–24] Specifically, performance metrics such as sensitivity, selectivity, or reproducibility of immunoassay platforms have been improved when combined with surface-enhanced Raman spectroscopy (SERS), a sensitive analytical technique for the detection of molecular fingerprints that has proven to be an excellent spectroscopic method.[25–28] Although Au spherical NPs or elongated nanorods have been frequently adopted as nanoprobes for SERS-based immunoassays to detect immunoreactions, it remains a great challenge to achieve highly reproducible and sensitive signals because of the random generation of hot spots with many Au spherical NPs.[29,30] In addition, the use of monometallic SERS-active NP components such as Au or Ag for immunoassays has intrinsic limitations including the low quality factor of Au due to damping of its surface plasmon resonance and an easy-oxidation of Ag (i.e., less biocompatibility), limiting their full utilization for practical immunoassays.[26,27,31,32]

Herein, we report the synthesis and application of biocompatible Ag@Au hollow DRNs for SERS-based immunoassay. The Ag@Au hollow DRNs are successfully synthesized by adopting multiple stepwise chemical reactions where Pt DRNs are used as a skeleton for building sequential Ag and Au coatings. The Ag@Au hollow DRNs show strong and reproducible SERS signals originating from the following contributions: (1) precisely tunable circular intra-nanogaps between outer and inner rims of DRNs, responsible for generating strong electromagnetic near-field focusing regardless of the polarization direction

of the incident light, (2) an underneath Ag layer with a higher optical quality factor, and (3) a chemically stable Au surface coating that prevents oxidation under corrosive biological environments for reproducible SERS signals. In addition, an open architecture of Ag@Au hollow DRNs allows for effective analyte capture at hot-zones, resulting in highly efficient immune-nanoprobes. As a proof-of-concept, we applied SERS-based immunoassay toward the detection of human chorionic gonadotropin (HCG) hormone, a biomarker for the diagnosis of pregnancy found at a highly elevated level in the urine of pregnant women.[33]

Results and discussion

Synthetic pathways for the synthesis of Ag@Au alloy DRNs

The synthetic procedure of Ag@Au hollow DRNs and the strategy of SERS-based immunoassays are schematically illustrated in Fig. 1.

By adopting triangular Au nanoplates as a starting material, multiple chemical steps including (1) shape-transformation into circular Au nanoplates through etching of protruded tips, (2) selective Pt deposition along the side of circular Au nanoplates, (3) inner Au etching and converting to Pt nanorings, (4) eccentric Au growth (i.e., Pt@Au nanorings), (5) a repetition of selective Pt deposition, and (6) inner Au etching are sequentially applied to successfully produce Pt DRNs where two Pt nanorings with different diameters are concentrically overlapped, forming circular intra-nanogaps between inner and outer rims. This "Preparation of Pt DRNs" multi-step synthetic pathway was executed by following our previous protocol (see Supplementary Note 1 in ESI† for details).[34] Size and morphological analyses for each sample using field-emission scanning electron microscopy (FE-SEM) are displayed in Fig. 2. Triangular Au nanoplates (Fig. 2A) were etched to circular Au nanoplates (Fig. 2B) by protruded
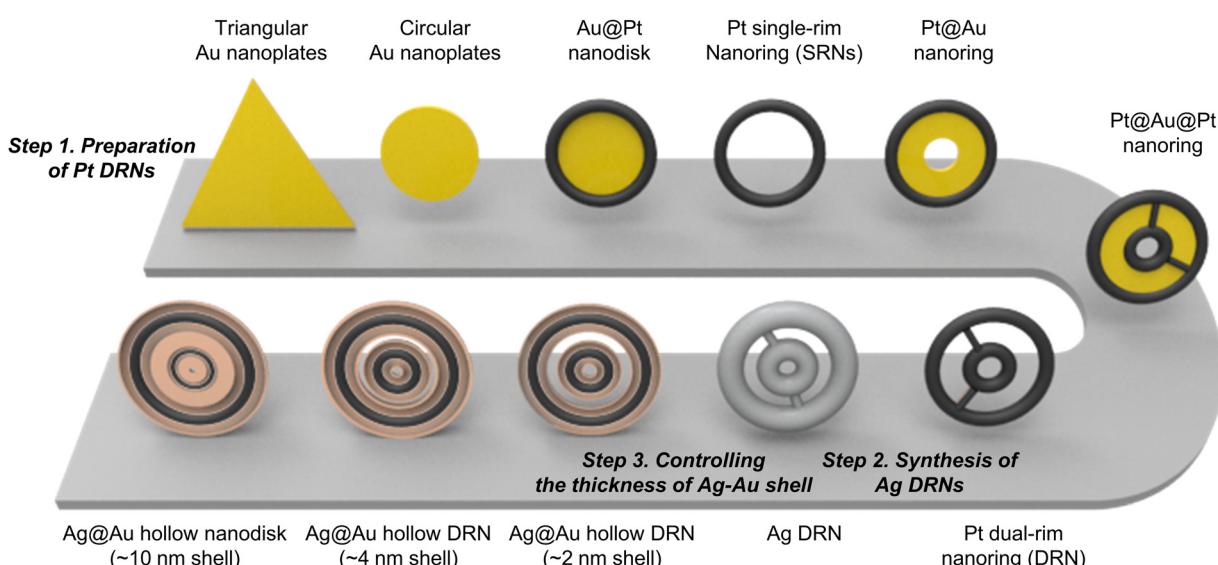

Fig. 1 Schematic illustration of the synthetic pathway of Ag–Au alloy DNRs. To synthesize Ag–Au alloy DNRs, multiple synthetic chemical steps are employed, including selective Pt deposition, inner Au etching, and concentric growth of Au onto Pt skeletons.
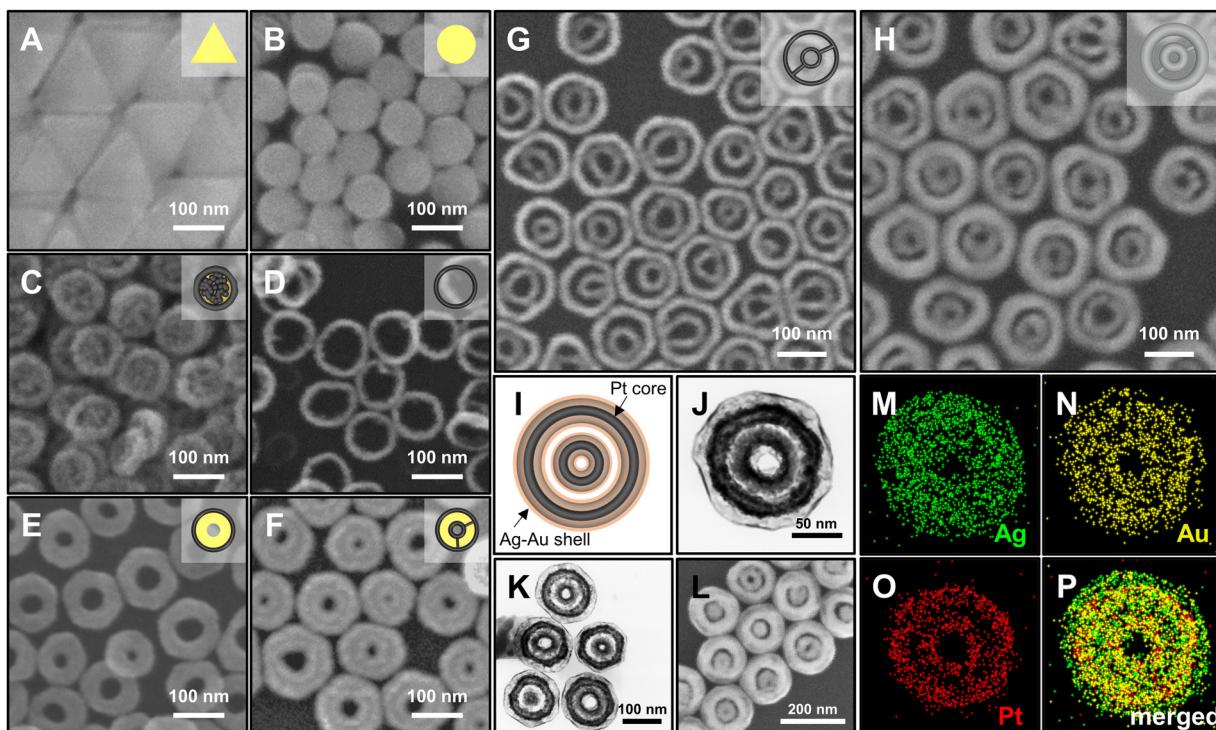
Fig. 2 Morphological evolution of bimetallic alloy Ag@Au hollow dual-rim nanorings (DRNs) using multi stepwise chemical reactions. FE-SEM images of (A) triangular Au nanoplates, (B) circular Au nanoplates, (C) Au@Pt nanodisks, (D) Pt single-rim nanorings, (E) Pt@Au nanorings, (F) Pt@Au@Pt nanorings, (G) Pt DRNs, and (H) Ag DRNs. (I–L) A schematic illustration, TEM images and an FE-SEM image of Ag@Au hollow DRNs. (M–P) EDS mapping images of an Ag@Au hollow DRN.

tip-selective etching with Au^{3+}. Then, edge-selective Pt deposition was applied to produce Au@Pt nanodisks with the assistance of a thin Ag layer (Fig. 2C) through galvanic replacement between Pt^{4+} and Ag, followed by inner Au etching by comproportionation of Au^+, leaving Pt single-rim nanorings (SRNs), as shown in Fig. 2D. The important step for the synthesis of Pt DRNs is the eccentric Au growth on Pt SRNs wherein Au grows in an inward fashion from the inner boundary of the Pt rims where residual Au adatoms at the periphery of the inner Pt rim facilitate reduction of Au under mild reducing conditions (i.e., using ascorbic acid) because of lattice mismatch between Pt and Au (the lattice constants of Pt and Au are 0.3912 nm, and 0.4065 nm, respectively), resulting in Pt@Au NRs (Fig. 2E). Repeating the selective Pt deposition on the inner Au domain and outer Pt domain (Fig. 2F), followed by selective etching of inner Au led to the formation of Pt DRNs where thin metal ligaments hold two inner and outer frames to maintain their double rim structures (Fig. 2G).

Morphological characterization of Ag@Au hollow DRNs

The Pt DRNs are utilized as a rigid core framework for the synthesis of Ag@Au hollow DRNs while keeping the circular intra-nanogaps between the inner and outer rims. First, Ag^+ is reduced on Pt DRNs in the presence of chloride counter-anions where the electrochemical potential ($E^{\circ}[Ag/AgCl]$ = 0.222 V) facilitates the fast kinetic growth conditions of Ag, leading to Ag reduction that concentrically wraps the Pt DRNs (Fig. 2H).[13,35] If we use bromide ions, a slow kinetic growth

condition occurred ($E^{\circ}[Ag/AgBr]$ = 0.071 V) where Ag fills the space between the outer rims and inner rims of Pt DRNs, resulting in merging circular intra-nanogaps, eventually leading to the formation of Ag SRNs instead of Ag DRNs (Fig. S1, ESI†). Then, Ag@Au hollow DRNs were prepared by the homogeneous wrapping of Ag DRNs with Au (Fig. 2I–L). Specifically, when we add Au^{3+} ions (15 nM) to the solution containing Ag DRNs with ascorbic acids (46 mM), the thin Au layer was deposited on the surface of the Ag surface ($\Delta E \sim 0.885$ V) without new nucleation in a solution. At the interface between the Ag core and Au shell, the Ag atoms diffuse faster into the outer Au layer than the outer layer Au to the Ag layer, leading to the formation of an alloy Ag and Au outer shell (Kirkendall process). During this replacement process, vacancies are generated in the Ag layer, moving toward the inner direction and coalescing into the hollow region to minimize the particle surface energy. As the Kirkendall process proceeds, the deposition of Au progressed until all the reducing agent was consumed. It is noteworthy that the nanoscale Galvanic exchange reaction is suppressed in the presence of ascorbic acid, under the given experimental conditions. In contrast, without ascorbic acid, the Galvanic replacement becomes dominant because of the difference in the redox potential of Au/ $AuCl_4^-$ ($E^{\circ}[Au/AuCl_4^-]$ = 1.002 V) and Ag/AgCl ($E^{\circ}[Ag/AgCl]$ = 0.222 V), which leads to concomitant oxidation and etching of the Ag layer and the reduction of Au^{3+}. As the Galvanic exchange reaction proceeded, Au debris were generated on the surface of the Ag template, resulting in an inhomogeneous DRN shape and

nanogaps (Fig. S2, ESI†). As shown in Fig. 2J–L, all resulting Ag@Au hollow DRNs show structurally well-defined circular intra-nanogaps. High-resolution transmission electron microscopy (HR-TEM) analysis revealed discernibly that there are two dark Pt cores in a concentric configuration with Ag–Au alloy shell wrapping and the bright hollow space, while narrow gaps between them were retained (Fig. 2J and K). The average sizes of the circular nanogaps decreased from 16 ± 3 nm in Pt DRNs to 13 ± 3 nm in Ag DRNs and to 5 ± 1 nm after Au deposition (see Fig. S3 for size distribution histograms of each DRN, ESI†). The energy-dispersive spectroscopy (EDS) mapping analysis shows atomic compositions of Ag, Au and Pt of 84%, 11% and 5%, respectively (Fig. 2M, N, O, and P, see Fig. S4 (ESI†) for EDS mapping images of Ag DNRs). Additionally, we monitored UV-vis-NIR spectra for each DRN (Pt DRNs, Ag DRNs, and Ag@Au hollow DRNs, Fig. S5, ESI†). The LSPR profile of Pt DRNs exhibited no spectral features due to plasmonically inactive Pt within the investigated spectral window (black trace). After the Ag deposition, the Ag DRNs showed an in-plane dipole mode at 824 nm and an out-of-plane dipole mode at 385 nm (blue trace), which is a characteristic feature of 2-dimensional nanoplates. After forming Ag@Au hollow DRNs, the in-plane dipole mode slightly blue-shifted to 820 nm, and the out-of-plane dipole mode redshifted to 403 nm (red trace) due to (1) a slight decrease in aspect ratio (from 4.7 for Ag DRNs to 4.3 for Ag@Au hollow DRNs) and (2) the formation of a Ag–Au alloy shell. In addition, the X-ray photoelectron spectroscopy (XPS) analysis of Ag@Au hollow DRNs showed a strong Ag 3d peak at 368.1 eV (Ag $3d_{5/2}$ peak and Ag $3d_{3/2}$ peak at 368.1 eV and 374.1 eV) and an Au 4f peak at 84.1 eV (Au $4f_{7/2}$ peak and Au $4f_{5/2}$ peak at 83.9 eV and 87.6 eV), further confirming the bimetallic surface composition (Fig. S6, ESI†).[36]

Single-particle SERS (spSERS) measurement of hollow DRNs toward detection of 2-naphthalenethiol (2-NTT)

To gain insight into the strong near-field focusing capabilities of Ag@Au hollow DRNs, single-particle SERS (spSERS) measurements were conducted (laser excitation wavelength: 785 nm, laser power: 170 µW) with 2-naphthalenethiol (2-NTT) as a Raman probe (Fig. 3 and Fig. S7, ESI†). Ag@Au hollow DRNs decorated with 2-NTT were randomly distributed on the transparent glass substrates (thickness ~0.13 mm), while the positions of each DRN were monitored by Rayleigh scattering images. After the spSERS measurement, we ensured that the SERS spectra were achieved from a single particle using FE-SEM images (see Fig. S8, ESI† and Experimental section for experimental details of spSERS measurement). Pure Au, Ag DRNs and Ag@Au hollow DRNs exhibit well-resolved spSERS signals (Fig. 3A–C). However, there were no detectable Raman features from analogous SRNs (Fig. S9, ESI†). As expected, the presence of nanogaps in a single entity is critical for focusing the near-field within those circular hot-zones (see Fig. S10 and S11 for FE-SEM images, and UV-vis-NIR spectra of Au DRNs and SRN analogues, ESI†). Since the quality factor of Ag was much larger than that of Au, the Ag DRNs showed a stronger spSERS signal compared to the Au DRNs when they have similar intra-nanogap sizes (~11 nm). Surprisingly, the spSERS intensity from Ag@Au hollow DNRs was 24.9 and 2.6 times higher than that of pure Au and Ag DRNs, respectively. The calculated enhancement factor, EF for Ag@Au hollow DRNs is ~1.4×10^9.

For comparison, we synthesized Ag@Au hollow DRNs with varying thicknesses of Ag–Au shell layer (~4 nm shell and ~10 nm shell) by tuning the concentration of Au precursor during Au growth on the Ag DNRs (30 nM and 75 nM, respectively) and studied their near-field focusing capabilities (see Fig. S12 for FE-SEM images, HR-TEM images, and UV-vis-NIR spectra of Ag@Au hollow DRNs with varying Ag–Au shell thicknesses, ESI†). As the thickness of the Ag–Au shell layer increased, the Ag/Au ratio of the Ag–Au shell layer decreased (from 1.94 to 1.65, Fig. S13, ESI†), and the near-field focusing capability of the Ag@Au hollow DRNs dramatically decreased, as represented by spSERS signal intensity (Fig. 3D and E). When the thickness of the Ag–Au shell layer was ~10 nm, Ag@Au hollow DRNs exhibited merged intraparticle nanogaps with no
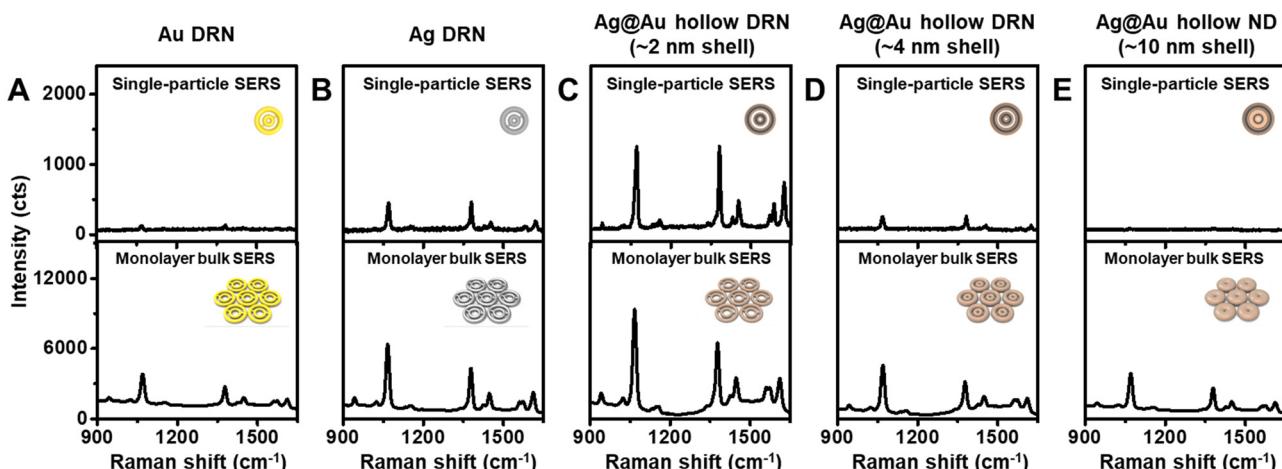

Fig. 3 Single-particle SERS and bulk SERS measurements. Single-particle SERS spectra and bulk SERS spectra of (A) Au DRNs, (B) Ag DRNs, (C) Ag@Au hollow DRNs (the thickness of Ag–Au shell: ~2 nm), (D) Ag@Au hollow DRNs (the thickness of Ag–Au shell: ~4 nm), and (E) Ag@Au hollow nanodisks (the thickness of Ag–Au shell: ~10 nm).

near-field focusing. It should be noted that the Ag–Au thin layer (∼2 nm) covering the Ag DNRs was thin enough for light to penetrate, allowing for the contribution of the Ag layer to the near-field focusing at the nanogaps, which is the optimum thickness for achieving strong light trapping in our current experimental conditions. Otherwise, we could not effectively utilize the high optical extinction of the Ag layer.

In addition, we investigated the near-field focusing capability of bulk SERS substrates in which 2D monolayers of SRNs and DRNs were prepared by the Langmuir–Blodgett (LB) method (Fig. S14, ESI†). The assembly consisting of SRNs showed recognizable SERS spectra because of the inter-particle coupling effect (unlike the spSERS cases) (Fig. S15, ESI†). When the DRNs were self-assembled into closed packing arrays, an increase of the SERS signals was obvious because of the enhanced near-field focusing capability due to the combinatorial synergistic effect from inter- and intra-particle couplings of each of the DRNs (Fig. 3). Specifically, the SERS intensity of the Ag@Au hollow DRNs assembly was the strongest among all investigated assemblies, indicating the ultrahigh sensitivity of Ag@Au hollow DRNs in bulk SERS systems.

Stability of Ag, Au and Ag@Au hollow DRNs under an oxidizing environment

We tested the stability of assembled Au DRNs, Ag DRNs and Ag@Au hollow DRNs by monitoring their SERS signals as a function of time when they were immersed in a highly oxidizing environment (5% H_2O_2) as certain biological environments and treatments could be corrosive and oxidizing as schematically described in Fig. 4A. From the FE-SEM images taken at 10 min-immersion, the rim thickness of Ag DRNs was reduced from 30 ± 3 nm to 22 ± 3 nm (*i.e.*, oxidizing) while the Au DRNs and Ag@Au hollow DRNs showed no structural deformation (Fig. 4B). This is more clearly observed in the time-dependent SERS spectra (Fig. 4C–E). It should be noted that the high Raman intensity of the 2D monolayer of Ag@Au hollow DRNs showed a slightly reduced intensity in the first 4 min due to unstable residual surface Ag being etched out. The Au DRNs also showed good stability, but their intensity was not as strong as the case of Ag@Au hollow DRNs. In contrast, in the case of the Ag DRNs, the SERS signals decreased even in 2 min and completely disappeared within 10 min due to the surface oxidation of Ag. This indicates the instability of Ag, which is
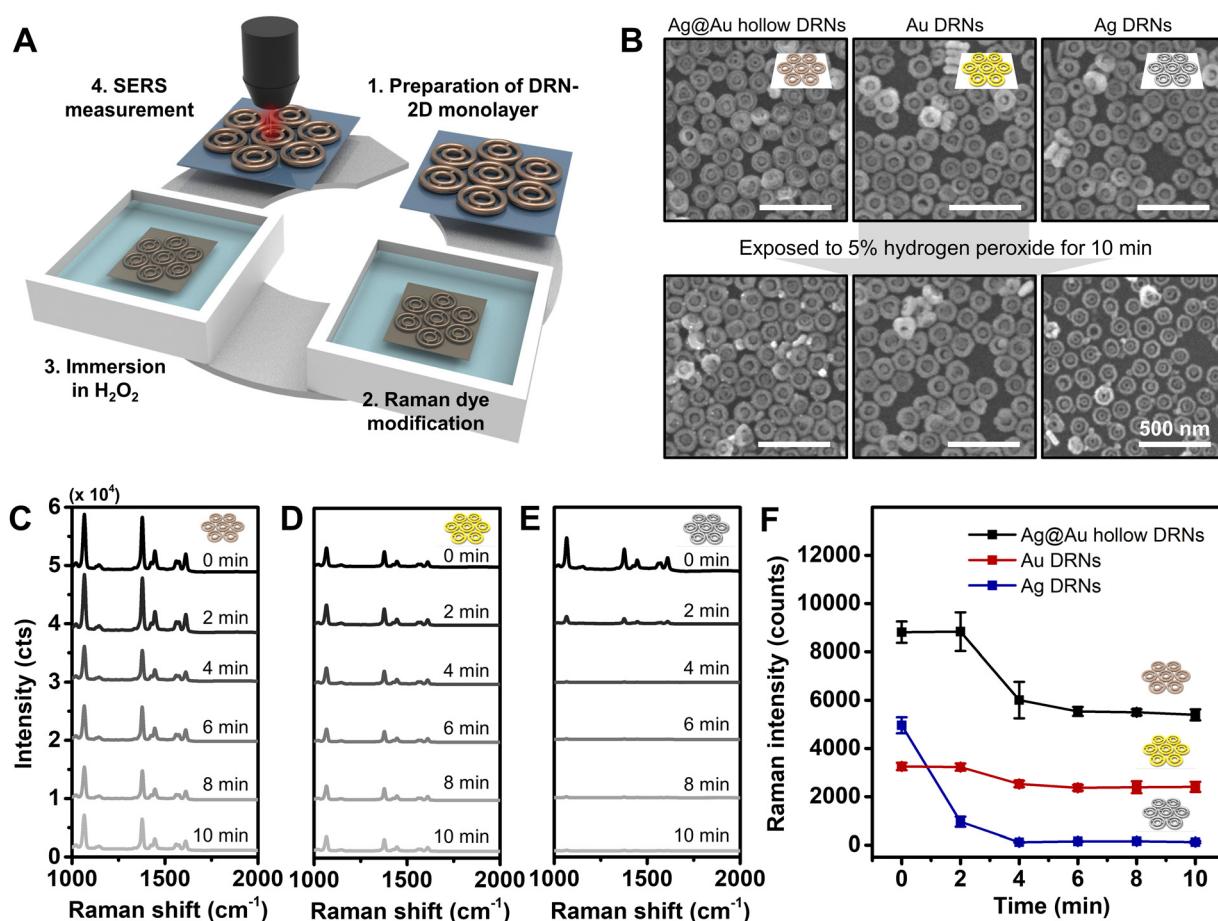

Fig. 4 Stability test of DRNs under the oxidizing conditions. (A) Schematic illustration of the experimental procedures for the stability test of DRNs. (B) FE-SEM images and (C–E) SERS spectra (F) and corresponding SERS intensity plot of the 2D monolayer of DRNs before and after being exposed to the 5% hydrogen peroxide condition. (Intensity was plotted based on the peak at 1069 cm^{-1}.) The error bars represent standard deviation ($n = 3$).
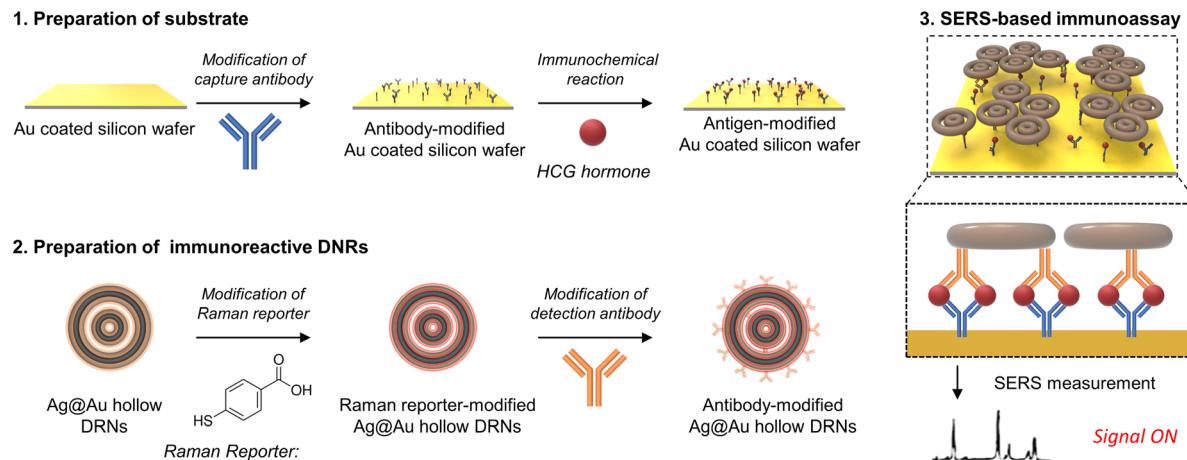
Fig. 5 Schematic illustration of the strategy of the SERS-based immunoassay. Antibody-modified Ag–Au DRNs are distributed onto human chorionic gonadotropin (HCG) bound Au-coated silicon wafers to form a sandwich formation measured by SERS.

not suitable for practical applications (Fig. 4F). Overall, our results demonstrate the excellence of Ag@Au hollow DRNs for potential SERS-immunoassay nanoprobes wherein highly stable and strong SERS signals are necessary.

SERS-based immunoassay with Ag@Au hollow DRNs and sensitivity comparison with a commercial lateral flow assay

Finally, we designed a sandwich assay to achieve a SERS-based immunoassay platform as schematically described in Fig. 5. We adopted capture antibody (Anti-HCG, mouse polyclonal antibody) modified Au-coated silicon wafers as a substrate, and target antigens (HCG hormones) were drop-cast on the wafers for immunochemical reactions.[37] Then, immunoreactive Ag@Au hollow DRNs were introduced to the antigen bound Au-coated silicon wafers and were incubated for 1 min. Finally, unreacted DRNs and non-specific antigens in the immunochemical reaction were washed out to ensure that only antigen–antibody specific binding was detected in the SERS spectra. Au-coated Si wafers were exploited for the substrate of SERS-based immunoassay, because of the easy surface modification of the substrate through Au-thiol chemistry and SERS signal enhancement, which was ascribed to the formation of nanogaps between Au-coated Si wafers and nanoparticles.

We conducted SERS mapping (scanned area: 200 μm × 200 μm, interval of 20 μm, integration time of 500 ms) and plotted the corresponding averaged-SERS spectra (laser excitation wavelength: 785 nm, laser power: 4 mW, see Fig. S16 for SERS mapping images, ESI†). Hollow DRNs conjugated with antibodies linked *via* 4-mercaptobenzoic acid (4-MBA) Raman active dye show two major characteristic peaks at 1080 cm^{-1} and 1580 cm^{-1}, which come from the ν_{8a} and ν_{12} aromatic ring vibration modes from 4-MBA, respectively.[38]

The SERS spectra of Ag@Au hollow DRNs as a function of HCG concentration are shown in Fig. 6A, demonstrating that the limit of detection (LOD) of Ag@Au hollow DRNs toward HCG detection is 10 pM, which indicates that our SERS-based platform with Ag@Au hollow DRNs is highly sensitive toward

HCG detection. As compared to the LODs of Au DRNs (1 nM) and Au nanospheres (1 nM, the diameter of Au nanosphere: 30 ± 5 nm) (Fig. 6B–D), the Ag@Au hollow DRNs provide effective and sensitive detection capability as bio-nanoprobes.

The generation of well-defined SERS signals is ascribed to the (1) circular intraparticle hot-zones in Ag@Au hollow DRNs responsible for strong electromagnetic near-field collection, (2) interparticle nanogaps among nanoparticles and (3) stable surface resistance to oxidation due to the presence of Au. When we applied Ag DRNs for HCG assay, the LOD was only 1 nM, owing to the low stability of Ag DRNs under the oxidizing sample-preparation environment despite the high optical extinction of Ag (Fig. S17, ESI†). It should be noted that the optimized intra-nanogap size of Ag@Au hollow DRNs for the best SERS-based immunoassay result was ~5 nm. The electromagnetic near-field could not be collected effectively (Fig. S18, ESI†) when the intra-nanogaps increased to 8 nm (or 10 nm). Additionally, considering that the LODs achieved from SRN analogues range from 1 nM to 10 nM with a narrow dynamic range (Fig. S19, ESI†), it is important to rationally design plasmonic constituents for achieving highly sensitive SERS-based immunoassays. Finally, the LOD of the commercially available lateral flow assay kit toward HCG detection is 500 nM (Fig. 6E), which is 4 orders higher than that of the Ag@Au hollow DRN system, implying the potential applicability of our system with bimetallic alloy DRN architectures.

Conclusions

In summary, we have reported highly sensitive and effective SERS-based immunoassays for the detection of HCG hormones using Ag@Au hollow DRNs wherein circular intra-nanogaps strongly collect an electromagnetic near-field, thereby enabling the ultrasensitive detection of target systems. The high chemical stability of Au complements the surface oxidation of Ag while preserving the high optical properties of Ag, resulting in a combinatorial effect with intra-nanogaps in a single entity.
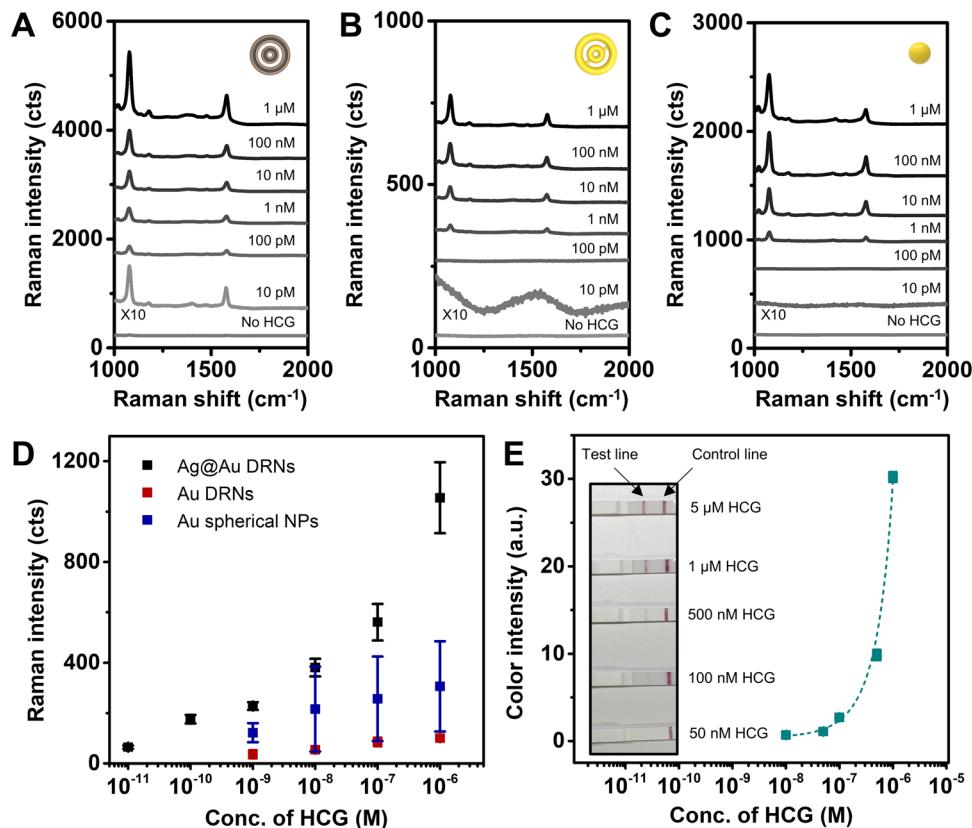
Fig. 6 SERS-based immunoassay with DRNs. SERS spectra obtained from SERS-based immunoassay with (A) Ag@Au hollow DRNs, (B) Au DRNs and (C) Au nanospheres for the detection of HCG hormones with different concentrations. (D) Calibration curves representing the relationship between Raman intensity and concentration of HCG hormones from the SERS-based immunoassay (the intensity plot was plotted based on the peak at 1080 cm^{-1}). (E) A calibration curve achieved from a lateral flow assay kit. The inset photograph exhibits the HCG detection result obtained from a commercially available pregnancy diagnosis kit where the appearance of two red bands both at the test line and the control line indicates pregnancy.

Plasmonic properties of Ag@Au hollow DRNs were systematically investigated by comparing them with single-component DRNs (Ag, or Au) as well as single rim analogues, demonstrating the superior SERS activity of Ag@Au hollow DRNs. For SERS-based immunoassays, the Ag@Au hollow DRNs showed a very low LOD of 10 pM toward HCG hormones, which is 4 orders lower than that (500 nM) of the commercially available lateral flow kit. We expect that our synthetic scheme for a highly complex nanoarchitecture and strategy for SERS-based immunoassay can be applied to sensitive and efficient detection of other types of viruses, bacteria and proteins.

Materials and methods

Chemicals and materials

Trisodium citrate dihydrate, sodium iodide ($\geq 99.5\%$), hexadecyltrimethylammonium bromide (CTAB, $\geq 98\%$), L-ascorbic acid (99%), TWEEN® 20, MES monohydrate ($\geq 99.0\%$), N-(3-dimethylaminopropyl)-N'-ethylcarbodiimide hydrochloride (EDC) ($\geq 98\%$), N-hydroxysuccinimide (NHS, 98%), 3-mercaptopropionic acid ($\geq 99\%$), phosphate buffered saline tablet, bovine serum albumin, human chorionic gonadotropin hormone, and 2-naphthalenethiol (99%) were purchased from Sigma-Aldrich.

Hydrogen tetrachloroaurate(III) hydrate (HAuCl$_4\cdot n$H$_2$O, 99%), hydrogen hexachloroplatinate(IV) hydrate (H$_2$PtCl$_6\cdot n$H$_2$O, 99%), and silver nitrate (AgNO$_3$, 99.9%) were purchased from Kojima, Japan. Sodium borohydride (NaBH$_4$, 98.0%) was purchased from Junsei, Japan. Hydrochloric acid (HCl, 35%), hydrogen peroxide (H$_2$O$_2$, 34.5%) and sodium hydroxide (NaOH, 98.0%) were purchased from Samchun, Korea. Hexadecyltrimethylammonium chloride (CTAC, $> 95.0\%$) was purchased from Tokyo Chemical Industry, Japan. 4-Mercaptobenzoic acid (90%), and HCG recombinant rabbit monoclonal antibody (RM330) were purchased from ThermoFisher Scientific. All reagents were dissolved in triply deionized water (≥ 18.2 MΩ) prepared by Milli-Q (from Millipore). Anti-HCG antibody (HCG1, mouse polyclonal antibody, ab400) was purchased from Abcam. A lateral flow assay-based pregnancy tester (WONDFO pregnancy test) was purchased from Guangzhou Wondfo Biotech Co., Ltd, China.

Synthesis of Ag dual-rim nanorings (DRNs)

We prepared Pt DRNs by following the experimental procedure reported previously.[12] We synthesized Ag DRNs by mixing 250 μL of Pt DRNs with 500 μL of 0.1 M CTAC, 200 μL 0.2 mM AgNO$_3$, 40 μL of 0.01 M ascorbic acid, and 20 μL of 0.05 M sodium hydroxide. After the reaction at 30 °C for 10 min,

we washed the resulting solution with triply deionized water twice *via* centrifugation at 12 000 rpm for 5 min. We tuned the rim thickness of the Ag DRNs by controlling the volume of 0.2 mM AgNO$_3$ solution.

Synthesis of Ag@Au hollow DRNs

We synthesized Ag@Au hollow DRNs by mixing 100 μL of Ag DRNs with 200 μL of 0.1 M CTAC, 300 μL of 0.1 M ascorbic acid, and 50 μL of 0.2 mM HAuCl$_4$. After the reaction at 30 °C for 5 min, we washed the resulting solution with triply deionized water twice *via* centrifugation at 12 000 rpm for 5 min. We tuned the intra-nanogap size (or the thickness of Ag–Au alloy shell) of the Ag@Au hollow DRNs by controlling the volume of 0.2 mM HAuCl$_4$ solution.

Synthesis of Ag@Au hollow SRNs

We synthesized Ag@Au alloy hollow SRNs by mixing 100 μL of Ag SRNs with 200 μL of 0.1 M CTAC, 300 μL of 0.1 M ascorbic acid, and 100 μL of 0.2 mM HAuCl$_4$. After the reaction at 30 °C for 5 min, we washed the resulting solution with triply deionized water twice *via* centrifugation at 12,000 rpm for 5 min.

Synthesis of Au SRNs

We synthesized Au SRNs by mixing 400 μL of Pt SRNs with 100 μL of 0.1 M CTAB, 300 μL of 0.1 M ascorbic acid, and 30 μL of 2 mM HAuCl$_4$ in the presence of iodide ion (50 μM). After the reaction at 70 °C for 15 min, we washed the resulting solution with triply deionized water twice *via* centrifugation. We tuned the rim thickness of Au SRNs by controlling the reaction time.

Surface modification of nanoparticles with detection antibodies

We modified the nanoparticles with detection antibodies (HCG recombinant rabbit monoclonal antibody (RM330)) for SERS-based immunoassays. To decorate the surface of the nanoparticles with 4-mercaptobenzoic acids, we mixed 100 μL of nanoparticles with 100 μL of 0.1 M CTAB and 50 μL of 1 mM 4-mercaptobenzoic acid solution (dissolved in 10% ethanol solution). After the reaction at 70 °C for 15 min, we washed the resulting solution *via* centrifugation at 12 000 rpm for 5 min to remove residual 4-mercaptobenzoic acid molecules. To immobilize detection antibodies at the surface of the nanoparticles, we conducted EDC/NHS coupling to activate the carboxylic acid functional group of 4-mercaptobenzoic acids immobilized at the surface of the nanoparticles. We added 100 μL of an EDC/NHS solution (800 μM of *N*-hydroxy-succinimide and 400 μM of *N*-(3-dimethylaminopropyl)-*N*′ethylcarbodiimide dissolved in MES buffer (pH 6.5) with TWEEN® 20 (0.5%)) to 100 μL of the nanoparticle solution. After the reaction at room temperature for 10 min, we washed the resulting solution with centrifugation at 12 000 rpm for 5 min to remove the residual EDC/NHS solution. To immobilize antibodies on the surface of the nanoparticles, we introduced 100 μL of antibodies (HCG recombinant rabbit monoclonal antibody, 1 : 10 000 dilution in PBS) to the carboxylic acid group activated nanoparticles. After the reaction at room temperature for 10 min, we washed the resulting solution with centrifugation at 12 000 rpm for 5 min to remove residual antibodies and dispersed them in PBS. The concentration of the NPs for immunoassays was fixed at 600 pM.

Surface modification of Au coated silicon wafer substrates with capture antibodies for immunoassays

We modified the Au-coated silicon wafers (4 mm, 4 mm, the thickness of Ti layer: 100 Å, the thickness of Au layer: 1000 Å) with capture antibodies for SERS-based immunoassays. To decorate the Au-coated silicon wafer, we cleaned the surface of the Au-coated silicon wafer through sonication in ethanol for 10 min. Then, we immersed the Au-coated silicon wafer in 0.1 M 3-mercaptopropionic acid solution to generate carboxylic acid functional groups at the surface of the Au-coated silicon wafers. After the reaction at room temperature for 6 h, we washed the surface with ethanol to remove residual 3-mercaptopropionic acid molecules. To activate carboxylic acid groups for the formation of amide bonding with capture antibodies, we conducted EDC/NHS coupling. We immersed a 3-mercaptopropionic acid decorated Au-coated silicon wafer in 20 mL of an EDC/NHS solution (80 mM of *N*-hydroxysuccin-imide and 40 mM of *N*-(3-dimethylaminopropyl)-*N*′-ethylcar-bodiimide dissolved in MES buffer (pH 6.5) with TWEEN 20 (0.5%)) for 30 min. After EDC/NHS coupling, we washed the Au-coated silicon wafers with PBS. To immobilize capture anti-bodies on the surface of the Au-coated silicon wafer, we dropped 4 μL of antibodies (Anti-HCG antibody, mouse poly-clonal antibody, 1 : 1000 dilution in PBS) on the carboxylic acid group activated Au-coated silicon wafer. After the reaction at room temperature for 30 min, we dropped 4 μL of 5% bovine serum albumin (BSA) solution on the Au-coated silicon wafer.

Experimental conditions for SERS-based immunoassay

We dropped 4 μL of HCG hormone (diluted with PBS) with varying concentrations of the capture antibody-modified Au-coated silicon wafer. This was incubated at room temperature for 10 min for immunochemical reactions between the antigens and capture antibodies modified on the Au-coated silicon wafer. After incubation, we dropped 4 μL of detection antibody-modified nanoparticles on the antigen-antibody modified Au-coated silicon wafer, which was incubated at room temperature for 1 min for immunochemical reactions between antigens immobilized on the Au-coated silicon wafer and detection antibodies on the nano-particles. After 1 min, we washed the Au-coated silicon wafer with PBS. After washing, we removed moisture on the silicon wafer with N$_2$ gas. Then, we conducted SERS mapping for immunoas-says (mapping area: 200 μm, 200 μm, with 20 μm interval). We monitored the 1080 cm^{-1} peak (aromatic ring vibration mode of 4-mercaptobenzoic acid) with a 785 nm laser (laser power: 4 mW) with an integration time of 500 ms.

Experimental conditions for single-particle SERS measurements

We measured single-particle SERS using a Raman microscope (Ntegra, NT-MDT) equipped with an inverted optical microscope

(IX 73, Olympus). A dichroic mirror directs the excitation laser beam into an oil-immersion objective lens (UPlanSApo, 100 ×, 1.4 numerical aperture), which focuses the beam to a diffraction-limited spot ($\sim 2 \mu m$) on the upper surface of the cover glass slip. We obtained photomultiplier tube images using a piezoelectric x, y sample scanner to identify nanoparticles. Samples were exposed to 50 mM 2-naphthalenethiol for 3 h. We obtained SERS spectra with a 785 nm laser (170 μW) for 10 s. We detected signals using a charge-coupled device detector (1024 × 256 pixels; Peltier cooled to −70 °C, Andor Newton DU920P BEX2-DD). To obtain SEM images of the nanoparticles on the cover glass after SERS measurements, we deposited a Pt layer on the cover glass with nanoparticles using an Ar plasma sputter-coater (Cressington 108 auto) with a current of 20 mA for 60 s.

Experimental conditions for bulk SERS measurements

We prepared a 2D monolayer of nanoparticles for bulk SERS measurements by the Langmuir–Blodgett method. We added 1 mL of samples into a Teflon bath and added 1 mL of hexane at the top surface of a nanoparticle solution to generate a hexane-water interface. Then, we added 1 mL of ethanol. After nanoparticles were transported from the solution to the hexane–water interface, we evaporated hexane at the top surface of the nanoparticle solution. We collected the 2D monolayer of nanoparticles on the silicon wafer. We immersed the 2D monolayer of nanoparticles on the silicon wafer in 0.01 M 2-naphthalenethiol (dissolved in ethanol) for 3 h to saturate the surfaces of the nanoparticles with analyte. Then, the samples were washed with ethanol for 5 min and dried for SERS measurements. We obtained SERS spectra (laser excitation wavelength: 785 nm, laser power: 4 mW, 20× objective lens, SERS mapping area: 50 μm × 50 μm, interval 10 μm) of 2-naphthalenethiol with an integration time of 1 s.

Instrumentation

We obtained images of nanoparticles using field-emission scanning electron microscopy (JSM-7100F, JEOL) and high-resolution transmission electron microscopy (JEM-ARM 200F, JEOL). We obtained UV-vis-NIR spectra using a UV-vis-NIR spectrophotometer (UV-3600, Shimadzu). We obtained Raman spectra and Raman mapping images using Raman microscopes including WiTec alpha 300R (for 532 and 633 nm laser excitation wavelengths), XperRAM-S700 (Nanobase, for 785 nm laser excitation wavelength), and NT-MDT (Ntegra, for single-particle SERS measurements).

Author contributions

S. P., Su. L., and I. J. conceived and designed the project. Su. L., So. L., J. L., and M. O. collected data. S. P., I. J., and Su. L. wrote the manuscript. Su. L., I. J., M. P., J. K., M. H., and W. P. contributed to the data analysis. All the authors approved the decision to submit for publication. All authors have given approval to the final version of the manuscript.

Conflicts of interest

There are no conflicts to declare.

Acknowledgements

References

1 H. X. Lin, S. M. Lee, L. Sun, M. Spellings, M. Engel, S. C. Glotzer and C. A. Mirkin, Clathrate colloidal crystals, *Science*, 2017, **355**(6328), 931–935.

2 T. Kwon, M. Jun and K. Lee, Catalytic Nanoframes and Beyond, *Adv. Mater.*, 2020, **32**, 33.

3 Z. Y. Wang, S. F. Zong, L. Wu, D. Zhu and Y. P. Cui, SERS-Activated Platforms for Immunoassay: Probes, Encoding Methods, and Applications, *Chem. Rev.*, 2017, **117**(12), 7910–7963.

4 M. Arabi, A. Ostovan, Z. Y. Zhang, Y. Q. Wang, R. C. Mei, L. W. Fu, X. Y. Wang, J. P. Ma and L. X. Chen, Label-free SERS detection of Raman-Inactive protein biomarkers by Raman reporter indicator: Toward ultrasensitivity and universality, *Biosens. Bioelectron.*, 2021, **174**, 112825.

5 H. Chen, S. G. Park, N. Choi, H. J. Kwon, T. Kang, M. K. Lee and J. Choo, Sensitive Detection of SARS-CoV-2 Using a SERS-Based Aptasensor, *ACS Sens.*, 2021, **6**(6), 2378–2385.

6 H. F. Liu, E. H. Dai, R. Xiao, Z. H. Zhou, M. L. Zhang, Z. K. Bai, Y. Shao, K. Z. Qi, J. Tu, C. W. Wang and S. Q. Wang, Development of a SERS-based lateral flow immunoassay for rapid and ultra-sensitive detection of anti-SARS-CoV-2 IgM/IgG in clinical samples, *Sens. Actuators, B*, 2021, **329**, 129196.

7 P. Zheng, M. Li, R. Jurevic, S. K. Cushing, Y. X. Liu and N. Q. Wu, A gold nanohole array based surface-enhanced Raman scattering biosensor for detection of silver(ı) and mercury(ıı) in human saliva, *Nanoscale*, 2015, **7**(25), 11005–11012.

8 H. Dang, S. G. Park, Y. Wu, N. Choi, J. Y. Yang, S. Lee, S. W. Joo, L. X. Chen and J. Choo, Reproducible and Sensitive Plasmonic Sensing Platforms Based on Au-Nanoparticle-Internalized Nanodimpled Substrates, *Adv. Funct. Mater.*, 2021, **31**(49), 2105703.

9 J. Reguera, J. Langer, D. J. de Aberasturi and L. M. Liz-Marzan, Anisotropic metal nanoparticles for surface

enhanced Raman scattering, *Chem. Soc. Rev.*, 2017, **46**(13), 3866–3885.

10 F. Qin, T. Zhao, R. B. Jiang, N. N. Jiang, Q. F. Ruan, J. F. Wang, L. D. Sun, C. H. Yan and H. Q. Lin, Thickness Control Produces Gold Nanoplates with Their Plasmon in the Visible and Near-Infrared Regions, *Adv. Opt. Mater.*, 2016, **4**(1), 76–85.

11 X. M. Cui, F. Qin, Q. F. Ruan, X. L. Zhuo and J. F. Wang, Circular Gold Nanodisks with Synthetically Tunable Diameters and Thicknesses, *Adv. Funct. Mater.*, 2018, **28**(11), 1705516.

12 T. H. Chow, Y. H. Lai, W. Z. Lu, N. N. Li and J. F. Wang, Substrate-Enabled Plasmonic Color Switching with Colloidal Gold Nanorings, *ACS Mater. Lett.*, 2020, **2**(7), 744–753.

13 S. Yoo, J. Lee, J. Kim, J. M. Kim, M. Haddadnezhad, S. Lee, S. Choi, D. Park, J. M. Nam and S. Park, Silver Double Nanorings with Circular Hot Zone, *J. Am. Chem. Soc.*, 2020, **142**(28), 12341–12348.

14 S. Lee, S. Lee, J. M. Kim, J. Son, E. Cho, S. Yoo, H. Hilal, J. M. Nam and S. Park, Au nanolenses for near-field focusing, *Chem. Sci.*, 2021, **12**(18), 6355–6361.

15 S. Lee, S. Lee, J. Son, J. M. Kim, J. Lee, S. Yoo, M. Haddadnezhad, J. Shin, J. Kim, J. M. Nam and S. Park, Web-above-a-Ring (WAR) and Web-above-a-Lens (WAL): Nanostructures for Highly Engineered Plasmonic-Field Tuning and SERS Enhancement, *Small*, 2021, **17**(31), 2101262.

16 J. M. Nam, J. W. Oh, H. Lee and Y. D. Suh, Plasmonic Nanogap-Enhanced Raman Scattering with Nanoparticles, *Acc. Chem. Res.*, 2016, **49**(12), 2746–2755.

17 T. Jiang, G. Chen, X. L. Tian, S. W. Tang, J. Zhou, Y. H. Feng and H. Y. Chen, Construction of Long Narrow Gaps in Ag Nanoplates, *J. Am. Chem. Soc.*, 2018, **140**(46), 15560–15563.

18 J. B. Song, B. Duan, C. X. Wang, J. J. Zhou, L. Pu, Z. Fang, P. Wang, T. T. Lim and H. W. Duan, SERS-Encoded Nanogapped Plasmonic Nanoparticles: Growth of Metallic Nanoshell by Templating Redox-Active Polymer Brushes, *J. Am. Chem. Soc.*, 2014, **136**(19), 6838–6841.

19 J. Shin, S. Lee, S. Yoo, I. Jung, S. Lee, J. Kim, J. Son, J.-E. Kim, J.-M. Kim, J.-M. Nam and S. Park, Enormous Enhancement in Single-Particle Surface-Enhanced Raman Scattering with Size-Controllable Au Double Nanorings, *Chem. Mater.*, 2022, **34**(5), 2197–2205.

20 X. L. Fu, L. X. Chen and J. Choo, Optical Nanoprobes for Ultrasensitive Immunoassay, *Anal. Chem.*, 2017, **89**(1), 124–137.

21 R. de la Rica and M. M. Stevens, Plasmonic ELISA for the ultrasensitive detection of disease biomarkers with the naked eye, *Nat. Nanotechnol.*, 2012, **7**(12), 821–824.

22 A. J. Haes, L. Chang, W. L. Klein and R. P. Van Duyne, Detection of a biomarker for Alzheimer's disease from synthetic and clinical samples using a nanoscale optical biosensor, *J. Am. Chem. Soc.*, 2005, **127**(7), 2264–2271.

23 B. V. Chikkaveeraiah, A. A. Bhirde, N. Y. Morgan, H. S. Eden and X. Y. Chen, Electrochemical Immunosensors for Detection of Cancer Protein Biomarkers, *ACS Nano*, 2012, **6**(8), 6546–6561.

24 W. B. Lu, Y. Wang, X. W. Cao, L. Li, J. Dong and W. P. Qian, Multiplexing determination of lung cancer biomarkers using electrochemical and surface-enhanced Raman spectroscopic techniques, *New J. Chem.*, 2015, **39**(7), 5420–5430.

25 T. Cotton, T. E. Rohr, N. Fan and P. J. Tarcha, Immunoassay employing surface enhanced Raman spectroscopy, *Anal. Biochem.*, 1989, **182**, 388–398.

26 Y. Cui, B. Ren, J. L. Yao, R. A. Gu and Z. Q. Tian, Synthesis of AgcoreAushell bimetallic nanoparticles for immunoassay based on surface-enhanced Raman spectroscopy, *J. Phys. Chem. B*, 2006, **110**(9), 4002–4006.

27 L. Wu, Z. Y. Wang, S. F. Zong, Z. Huang, P. Y. Zhang and Y. P. Cui, A SERS-based immunoassay with highly increased sensitivity using gold/silver core-shell nanorods, *Biosens. Bioelectron.*, 2012, **38**(1), 94–99.

28 Y. W. Pei, Z. Y. Wang, S. F. Zong and Y. P. Cui, Highly sensitive SERS-based immunoassay with simultaneous utilization of self-assembled substrates of gold nanostars and aggregates of gold nanostars, *J. Mater. Chem. B*, 2013, **1**(32), 3992–3998.

29 M. Li, J. W. Kang, S. Sukumar, R. R. Dasari and I. Barman, Multiplexed detection of serological cancer markers with plasmon-enhanced Raman spectro-immunoassay, *Chem. Sci.*, 2015, **6**(7), 3906–3914.

30 X. F. Zhang and X. Z. Du, Carbon Nanodot-Decorated Ag@SiO2 Nanoparticles for Fluorescence and Surface-Enhanced Raman Scattering Immunoassays, *ACS Appl. Mater. Inter.*, 2016, **8**(1), 1033–1040.

31 R. G. Sanedrin, D. G. Georganopoulou, S. Park and C. A. Mirkin, Seed-mediated growth of bimetallic prisms, *Adv. Mater.*, 2005, **17**(8), 1027.

32 Y. Yang, J. Y. Liu, Z. W. Fu and D. Qin, Galvanic Replacement-Free Deposition of Au on Ag for Core-Shell Nanocubes with Enhanced Chemical Stability and SERS Activity, *J. Am. Chem. Soc.*, 2014, **136**(23), 8153–8156.

33 K. Kerman, N. Nagatani, M. Chikae, T. Yuhi, Y. Takamura and E. Tamiya, Label-free electrochemical immunoassay for the detection of human chorionic gonadotropin hormone, *Anal. Chem.*, 2006, **78**(15), 5612–5616.

34 S. Yoo, J. Kim, S. Choi, D. Park and S. Park, Two-dimensional nanoframes with dual rims, *Nat. Commun.*, 2019, **10**, 5789.

35 J. Lee, S. Lee, J. Kim, S. Yoo, S. Lee, J. Son, H. Hilal, S. Go, J. Lee, J. M. Nam and S. Park, Synthesis of morphology controlled PtAu@Ag nanorings through concentric and eccentric growth pathways, *Chem. Commun.*, 2021, **57**(81), 10616–10619.

36 L. Shang, L. H. Jin, S. J. Guo, J. F. Zhai and S. J. Dong, A Facile and Controllable Strategy to Synthesize Au-Ag Alloy Nanoparticles within Polyelectrolyte Multi layer Nanoreactors upon Thermal Reduction, *Langmuir*, 2010, **26**(9), 6713–6719.

37 H. Hilal, Q. Zhao, J. Kim, S. Lee, M. Haddadnezhad, S. Yoo, S. Lee, W. Park, W. Park, J. Lee, J. W. Lee, I. Jung and S. Park, Three-dimensional nanoframes with dual rims as nanoprobes for biosensing, *Nat. Commun.*, 2022, **13**, 4813.

38 A. Michota and J. Bukowska, Surface-enhanced Raman scattering (SERS) of 4-mercaptobenzoic acid on silver and gold substrates, *J. Raman Spectrosc.*, 2003, **34**(1), 21–25.